



The TeV Spectral Bump of Cosmic-Ray Protons and Helium Nuclei: The Role of Nearby Supernova Remnants

Sourav Bhadra^{1,2} , Satyendra Thoudam³ , Biman B. Nath¹, and Prateek Sharma²

¹Raman Research Institute, Sadashiva Nagar, Bangalore 560080, India; sbhadra07@gmail.com

²Department of Physics, Indian Institute of Science, Bangalore 560012, India

³Department of Physics, Khalifa University of Science and Technology, PO Box 127788, Abu Dhabi, United Arab Emirates; satyendra.thoudam@ku.ac.ae

Received 2024 May 12; revised 2025 June 16; accepted 2025 June 22; published 2025 August 5

Abstract

The existence of nearby discrete cosmic-ray (CR) sources can lead to many interesting effects on the observed properties of CRs. Recent measurements of CRs with the CALET and the DAMPE experiments have revealed a bump-like new feature in the proton and helium spectra in the energy range $\sim(1\text{--}100)\text{ TeV n}^{-1}$. The origin of the feature is not clearly understood. In this paper, considering an improved and more detailed analysis than previous works, and using updated age and distance estimates of nearby supernova remnants (SNRs) along with an energy-dependent escape process for CRs from the remnants, we show that the spectral bump can be explained by the contribution of CRs from the nearby SNRs, in particular the Vela remnant. We also show that the contribution from the nearby remnants agrees well with the observed spectra of the heavier CR elements from carbon to iron, as well as with the measured all-particle CR spectrum beyond the knee region when combined with a background flux of CRs originating from distant SNRs.

Unified Astronomy Thesaurus concepts: Galactic cosmic rays (567); Particle astrophysics (96); Shocks (2086); Supernova remnants (1667)

1. Introduction

Cosmic rays (CRs) represent high-energy charged particles spanning a broad energy spectrum from 1 GeV to $\sim 10^{11}$ GeV. Supernova remnants (SNRs) have long been considered as the most promising sources of CRs in the Galaxy, particularly up to a few PeV (P. O. Lagage & C. J. Cesarsky 1983). Based on the fundamental principles of the diffusive shock acceleration (DSA) theory of CRs (W. I. Axford et al. 1977; R. D. Blandford & J. P. Ostriker 1978) and the nature of CR transport in the Galaxy, CRs are expected to follow a power-law spectrum. This prediction is in general good agreement with the measured CR spectrum at the Earth, which has an index of ~ -2.7 up to approximately 3×10^6 GeV (3 PeV), commonly referred to as the CR “knee.” The spectrum steepens to ~ -3.1 above the knee, possibly due to the subsequent cutoffs in the energy spectra of the different CR elements (S. Thoudam et al. 2016). The spectrum then flattens back to ~ -2.7 at 4×10^9 GeV, a feature known as the CR “ankle,” which is possibly caused by the interaction of extragalactic protons with cosmic microwave background (CMB) photons producing electron–positron pairs (V. S. Berezhinskii & S. I. Grigor’eva 1988) or due to the photodisintegration of CRs inside compact extragalactic sources (N. Globus et al. 2015; M. Unger et al. 2015). At $\sim 10^{11}$ GeV, the spectrum shows a steepening, the so-called “Greisen–Zatsepin–Kuzmin cutoff,” which can be the result of extragalactic CRs interacting with the CMB producing photopions (K. Greisen 1966; G. T. Zatsepin & V. A. Kuz’min 1966).

Several additional distinctive features have been discovered in the spectra of the individual CR elements below the knee energy. In this paper, we focus on the recent observations of a bump-like feature in the spectra of protons and helium nuclei

by the DAMPE (Q. An et al. 2019; F. Alemanno et al. 2021) and the CALET (O. Adriani et al. 2022a, 2023) experiments. This feature exhibits a hardening in the spectra at a few hundred GeV, confirming earlier detections by the PAMELA (O. Adriani et al. 2011) and the AMS-02 (M. Aguilar et al. 2015a, 2015b) experiments, followed by a subsequent softening above around 10 TeV n^{-1} . Various explanations for the spectral hardening have been proposed which are based on physical mechanisms that can affect the CR source spectrum (P. L. Biermann et al. 2010; Y. Ohira et al. 2011; Q. Yuan et al. 2011; V. Ptuskin et al. 2013) and the CR propagation properties in the Galaxy (P. Blasi et al. 2012; N. Tomassetti 2012; S. Thoudam & J. R. Hörandel 2014), as well as explanations based on the presence of nearby sources (A. D. Erlykin & A. W. Wolfendale 2012; S. Thoudam & J. R. Hörandel 2012a, 2013; G. Bernard et al. 2013). However, a convincing explanation for the origin of the spectral bump is still lacking.

Current explanations for the spectral bump are based on a multicomponent origin of CRs involving nearby sources. For instance, C. Yue et al. (2019) proposed the existence of multiple CR components originating from different populations of distant and nearby sources, while M. A. Malkov & I. V. Moskalenko (2021) proposed the presence of nearby Epsilon Indi or Epsilon Eridani stars as the origin of the bump, and A. Li et al. (2024) explained it on the basis of the presence of nearby SNRs. In this work, we also present an explanation based on nearby SNRs, but we bring several improvements over the other existing works. We consider a similar set of potential nearby SNRs that have previously been considered in S. Thoudam & J. R. Hörandel (2012a) to explain the spectral hardening observed at a few hundred GeV. We calculate the CR flux from the nearby SNRs in the presence of a background flux from the distant sources, where we use updated ages and distances of the nearby SNRs, a consistent spectral index for the CR source spectrum between the background and the



Original content from this work may be used under the terms of the [Creative Commons Attribution 4.0 licence](https://creativecommons.org/licenses/by/4.0/). Any further distribution of this work must maintain attribution to the author(s) and the title of the work, journal citation and DOI.

nearby flux components, finite sizes of the nearby SNRs in contrast to the commonly assumed point-like approximation, and a time-dependent escape for CRs of different energies from the remnants, unlike other works focusing on the spectral bump.

The effect of source discreteness on the observed spectra of CR nuclei has also been investigated, for example, in I. Büsching et al. (2005), A. W. Strong et al. (2009), and A. Stall et al. (2025) in a different context. Studies of the effect on the electron spectrum can be found in C. Y. Mao & C. S. Shen (1972) and R. Cowsik & M. A. Lee (1979), and later in T. Kobayashi et al. (2004), P. Mertsch (2011), and S. Thoudam & J. R. Hörandel (2012b).

The paper is organized as follows. In Section 2, we describe our model, and present the calculations of the CR fluxes from the nearby and the distant sources. We present the main results in Section 3, the discussion of our findings in Section 4, and the conclusion in Section 5.

2. The Model

It is widely accepted that SNRs are the major accelerators of CRs in the Galaxy (e.g., P. O. Lagage & C. J. Cesarsky 1983; W. I. Axford 1994), which is supported both by theoretical and observational evidence. Theoretically, it has been established that supernova shocks can accelerate suprathermal particles of the interstellar medium (ISM) to very high energies through the DSA process (W. I. Axford et al. 1977; A. R. Bell 1978; R. D. Blandford & J. P. Ostriker 1978). In addition, observational evidence comes from the detection of nonthermal radio and X-ray emissions (J. Vink & J. M. Laming 2003; E. Parizot et al. 2006) as well as GeV to TeV gamma rays from a number of SNRs (M. Ackermann et al. 2013; H. E. S. S. Collaboration et al. 2018a). Based on this evidence, we consider SNRs as the main sources of CRs, at least up to an energy of a few PeVs.

In our model, we consider two distinct components of the CRs observed at the Earth: a steady background which dominates the observed flux at most energies, and a time-dependent local component contributed by nearby sources (see, e.g., S. Thoudam & J. R. Hörandel 2013). The background CR component is assumed to originate from distant SNRs distributed uniformly throughout the Galactic disk. In contrast, the local component is considered to be produced from nearby SNRs that are within ~ 1 kpc of the Earth. The nearby SNRs considered in this work are listed in Table 1 along with their estimated ages and distances from the Earth. S. Thoudam (2006) showed that sources located mainly within ~ 1 kpc can produce a noticeable variation in the CR flux at the Earth.

The diffusion region for the background CRs is considered to have a cylindrical geometry with a vertical boundary at $\pm H$, and no boundary in the radial direction (see Figure 1 for a schematic). This is a reasonable assumption as far as the CRs at the Galactocentric position of the Sun is concerned because the majority of them are produced from sources located within a radial distance close to H from the Sun (S. Thoudam 2008). The precise value of H remains uncertain. Estimates derived from various CR propagation models span a wide range of ~ 2 – 12 kpc (A. W. Strong & I. V. Moskalenko 1998; W. R. Webber & A. Soutoul 1998). We consider a typical value of $H = 5$ kpc for the present analysis. In contrast, for the local CR component, we assume a diffusion region that is not

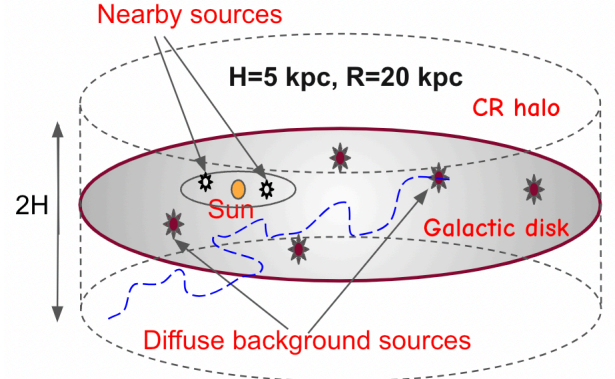


Figure 1. Schematic of the distribution of background and nearby SNRs on the Galactic plane. The encircled region around the Sun depicts the 1 kpc size region within which the nearby SNRs considered in this work are located. The blue dashed line illustrates the propagation of CRs from an SNR.

Table 1
List of Supernova Remnants within a Distance of 1 kpc from the Earth Considered in This Work

| SNR Name | Distance (kpc) | Age (yr) | References |
|-------------|----------------|-------------------|------------|
| Geminga | 0.25 | 3.4×10^5 | (1), (2) |
| Loop I | 0.17 | 2×10^5 | (3) |
| Vela | 0.30 | 10^4 | (4) |
| Monogem | 0.30 | 6.8×10^4 | (5) |
| Cygnus Loop | 0.73 | 2×10^4 | (6) |
| G 114.3+0.3 | 0.70 | 8×10^3 | (7) |
| Vela Junior | 0.70 | 3.7×10^3 | (8), (9) |
| S147 | 0.90 | 3×10^4 | (10) |
| HB 9 | 0.80 | 8×10^3 | (11) |
| HB 21 | 0.80 | 1.5×10^4 | (12) |
| SN 185 | 0.95 | 1.8×10^3 | (13) |

References. (1) J. Faherty et al. (2007); (2) H. E. S. S. Collaboration et al. (2023); (3) C. Dickinson (2018); (4) I. Sushch et al. (2011); (5) C. V. Cappiello et al. (2023); (6) R. A. Fesen et al. (2018); (7) A. Yar-Uyaniker et al. (2004); (8) N. I. Maxted et al. (2018); (9) E. G. Berezhko et al. (2009); (10) V. V. Gvaramadze (2006); (11) D. A. Leahy & W. W. Tian (2007); (12) J. S. Lazendic & P. O. Slane (2006); (13) H. E. S. S. Collaboration et al. (2018b).

constrained by any spatial boundary. This assumption is justified because the CR flux from the nearby sources remains largely unaffected by the presence of both the vertical and radial boundaries because of the very short propagation time of CRs to the Earth. The diffusive propagation time for CRs in the Galaxy follows $t_d \propto r^2/D$, where r is the average distance covered and D is the CR diffusion coefficient. Using this, one can easily check that the CR propagation time to the Earth from a source located 1 kpc away is a factor 0.04 smaller than the escape time from the Galaxy (considering a halo boundary of $H = 5$ kpc).

2.1. Cosmic Rays from Nearby Sources

After acceleration at supernova shocks, CRs eventually escape and undergo diffusive propagation through the ISM. The transport of CRs originating from a single nearby SNR

can be described by a time-dependent diffusion equation as

$$\nabla \cdot (D \nabla N_p) + Q = \frac{\partial N_p}{\partial t}, \quad (1)$$

where $N_p(r, E, t)$ denotes the number density of CR primary particles of kinetic energy per nucleon E at a distance r from the SNR at a given time t after the supernova explosion, $D(E)$ is the diffusion coefficient of CRs in the Galaxy, and $Q(r, E, t) = q(r)q(E)q(t)$ is the source term denoting the CR injection rate per unit volume from the SNR. In Equation (1), we neglect CR losses due to nuclear interactions with the interstellar matter since the time for CRs to reach the Earth from the nearby SNR is expected to be much less than the nuclear interaction timescale. For instance, for a typical interstellar matter density of $n_H \approx 1 \text{ H cm}^{-3}$, the interaction time for CR protons is $t_{pp} \approx (n_H \sigma c)^{-1} \sim 30 \text{ Myr}$, where c is the velocity of light. This is larger than the diffusive propagation time $t_d \approx r^2/4D \sim 0.3 \text{ Myr}$ for 1 TeV protons to the Earth from a source located at 1 kpc (see Section 2.2 for references to the interaction cross section σ , and Section 2.3 for the CR diffusion coefficient $D(E)$). As we focus mainly on high energies in this work, we also neglect effects that are important mostly for CRs at low energies (below $\sim 10 \text{ GeV}$) such as reacceleration, ionization losses, and convection by the Galactic wind. In addition, we neglect the production of CR secondaries (if any) inside the remnant from the interaction of the primary CRs before they are released into the ISM.

In the standard theory of DSA applied to SNRs, charged particles undergo acceleration each time they traverse the supernova shock front (W. I. Axford et al. 1977; A. R. Bell 1978; R. D. Blandford & J. P. Ostriker 1978). During the acceleration, the majority of particles are carried downstream of the shock and are unable to undergo further acceleration, whereas a small fraction diffuses upstream before being recaptured by the expanding shock and continuing with acceleration. This is true mostly during the free-expansion phase of the SNR evolution where the shock moves at a uniform speed with its radius increasing linearly proportional to time, whereas the displacement of particles undergoing a random walk grows proportional to the square root of time. However, during the Sedov phase, when the shock slows down, the upstream diffusing particles can begin to escape the remnant. Generally, particles are considered to escape the remnant when the upstream diffusion length D_u/v_s is larger than the escape boundary ξR_s , where D_u is the upstream diffusion coefficient, (v_s, R_s) are the velocity and radius of the shock, both a function of the SNR age, and the constant $\xi \ll 1$ (see, e.g., M. A. Malkov & L. O. Drury 2001; L. O. C. Drury 2012). In the Bohm diffusion limit, where the lowest value of the diffusion coefficient is achieved, $D_u \propto E/B_u$, and using the escape condition, we get $E_{\text{esc}} \propto B_u R_s v_s$ for the energy of the escaping CRs. During the Sedov phase, $R_s \propto t^{0.4}$ and $v_s \propto t^{-0.6}$, then the escape energy decreases (weakly) with time as $E_{\text{esc}} \propto t^{-0.2}$. If magnetic field amplification is taken into account, as suggested (H. J. Völk et al. 2005; D. Caprioli et al. 2009), the escape energy can have a stronger time dependence. A magnetic field in the presence of such an amplification scales with the shock velocity as $B_u \propto v_s^d$, where d is a positive constant, which can reach a value of 1.5 (A. R. Bell 2004). With this, we get the escape energy decreasing with time as $E_{\text{esc}} \propto t^{-(0.2+0.6d)}$.

Considering that the magnetic field amplification and nature of the magnetic turbulence are poorly understood, a simple but reasonable approach is to parameterize the escape energy as (S. Gabici et al. 2009; Y. Ohira et al. 2011; S. Thoudam & J. R. Hörandel 2012b)

$$E_{\text{esc}} = E_{\text{max}} \left(\frac{t}{t_{\text{sed}}} \right)^{-\alpha}, \quad (2)$$

where α is a positive constant. Equation (2) assumes that the particles with the highest energy E_{max} escape at the onset of the Sedov phase t_{sed} , followed by the lower-energy particles at later times when the shock becomes weak (S. Thoudam & J. R. Hörandel 2012b).

From Equation (2), we can write the CR escape time as a function of energy as

$$t_{\text{esc}} = t_{\text{sed}} \left(\frac{AE}{Ze\rho_m} \right)^{-1/\alpha}, \quad (3)$$

where E is the kinetic energy per nucleon, $\rho_m = 1 \text{ PV}$ is the maximum rigidity (E. G. Berezhko 1996), and $\alpha = 2.4$ as determined by the spectral fit performed in S. Thoudam & J. R. Hörandel (2013). It may be noted that the magnetic field amplification level ($d = 1.5$) as suggested by A. R. Bell (2004) corresponds to a value of $\alpha = 1.1$ for a Bohm-like diffusion. In our model, the time-dependent escape of CRs is crucial to explain the spectral hardening of protons and heavier nuclei observed at a few hundred GeVs by several experiments. Equation (3) implies that for the same energy/nucleon, heavy nuclei escape at a relatively early time compared to protons, with a timescale that is shorter by a factor of $(A/Z)^{-1/\alpha}$.

As discussed above, SNRs can effectively confine high-energy particles during the early stage of their evolution. At a later stage, when the shock slows down and cannot efficiently accelerate particles, it can no longer effectively confine the particles. We assume that all the low-energy particles escape the remnant at 10^5 yr when the shock becomes too weak. In our model, this happens at energies below $\sim 3 \text{ GeV}$ for protons (for details on the mechanism of particle escape from SNRs, see, e.g., D. Caprioli et al. 2009 and references therein). The CR escape time in our model is then considered as $T_{\text{esc}} = \min [t_{\text{esc}}(E), 10^5 \text{ yr}]$. The corresponding escape radii can be calculated using the age–radius Sedov relation for SNRs as given below (S. Thoudam & J. R. Hörandel 2013):

$$R_{\text{esc}} = 2.5 v_0 t_{\text{sed}} \left[\left(\frac{T_{\text{esc}}}{t_{\text{sed}}} \right)^{0.4} - 0.6 \right], \quad (4)$$

where v_0 is the initial shock velocity. We consider the SNR to be spherically symmetric. Assuming that CRs are uniformly distributed on the surface of the SNR before they are released, the source term in Equation (1) is written as

$$Q(r, E, t) = \frac{q(E)}{4\pi R_{\text{esc}}^2} \delta(r - R_{\text{esc}}) \delta(t - T_{\text{esc}}), \quad (5)$$

where $q(E)$ is the source spectrum, which can be expressed in terms of the total kinetic energy of the particle, $U = AE$, as

follows:

$$q(E) = Aq(U) = Ak \times (U^2 + 2Um)^{-(\gamma+1)/2} (U + m), \quad (6)$$

with m representing the rest-mass energy of the particle, γ the source spectral index, and k a constant related to the CR injection efficiency, which is defined as the fraction f of the supernova kinetic energy of 10^{51} erg injected into a given CR species. The solution of Equation (1) follows (S. Thoudam & J. R. Hörandel 2012b):

$$N_p(r, E, t) = \frac{q(E)R_{\text{esc}}}{rA_{\text{esc}}\sqrt{\pi D(t - T_{\text{esc}})}} \exp\left[-\frac{R_{\text{esc}}^2 + r^2}{4D(t - T_{\text{esc}})}\right] \times \sinh\left[\frac{rR_{\text{esc}}}{2D(t - T_{\text{esc}})}\right], \quad (7)$$

where $A_{\text{esc}} = 4\pi R_{\text{esc}}^2$ is the surface area of the SNR at the instant when CRs of kinetic energy/nucleon E escape the remnant. Equation (7) is valid only for time $t \geq T_{\text{esc}}$. The CR flux from the source at $t < T_{\text{esc}}$ is taken to be zero.

The onset of the Sedov time depends on the initial shock velocity of the SNR (v_0), the initial ejecta mass (M_{ej}), and the ambient ISM density (ρ) as $t_{\text{sed}} \approx (3M_{\text{ej}}/4\pi\rho)^{1/3}v_0^{-1}$. Typical values of Sedov time lie in the range $\sim 10^2$ – 10^3 yr. We consider a uniform value of $t_{\text{sed}} = 500$ yr for all of the nearby SNRs (S. Thoudam & J. R. Hörandel 2013). This gives the CR escape time in our model a range of $T_{\text{esc}} = (500$ – $10^5)$ yr depending on the energy, and a corresponding escape radius $R_{\text{esc}} \sim (5$ – $100)$ pc for a typical shock velocity of $v_0 = 10^4$ km s $^{-1}$. We assume all the nearby SNRs share the same set of model parameters $\{q(E), T_{\text{esc}}(E), R_{\text{esc}}(E)\}$. Additionally, in our model we consider the same CR source index for the nearby and the background sources.

2.2. Cosmic Rays from The Background Sources

The flux of the background primary CR component can be calculated from the time-independent (steady-state) propagation equation (S. Thoudam & J. R. Hörandel 2013):

$$\nabla \cdot [D \nabla N_p(E)] - \eta v_p \sigma_p \delta(z) N_p(E) = -Q_p(E), \quad (8)$$

where $N_p(\mathbf{r}, E)$ represents the CR number density with kinetic energy/nucleon E in cylindrical coordinate $\mathbf{r} = (r, z)$ with the center at the Galactic center position. The first term of Equation (8) represents diffusion, and the second term represents catastrophic loss due to collisions of CRs with ISM particles, where η is the averaged surface density of interstellar matter in the Galactic disk, v_p is the velocity, and $\sigma_p(E)$ is the inelastic collision cross section of the primary CR particles. We consider a uniform distribution of the background sources, represented by $Q_p(\mathbf{r}, E) = Sq(E)\delta(z)$, where S is the supernova explosion rate per unit surface area in the Galactic disk, and $q(E)$ is the source spectrum defined by Equation (6). We use the same source index for the background and the local components, but allow them to have different CR injection efficiencies considering the uncertainties in the supernova rate in the Galaxy. The solution of Equation (8) at $\mathbf{r} = 0$ is given by

(S. Thoudam & J. R. Hörandel 2013)

$$N_p(0, 0, E) = \frac{RSq_p(E)}{2D_p} \times \int_0^\infty \frac{J_1(KR)}{K \coth(KH) + \frac{\eta v_p \sigma_p}{2D_p}} dK, \quad (9)$$

where J_1 denotes a Bessel function of first order and R is the radial extent of the source distribution, which is taken to be 20 kpc. The collision cross section has been taken from S. Thoudam & J. R. Hörandel (2013), which is based on the cross sections reported in S. R. Kelner et al. (2006) for the protons and J. R. Letaw et al. (1983) for the heavier nuclei.

Primary CRs produce secondary particles due to their interaction (spallation) with ISM particles during their propagation in the Galaxy. The secondary CR production rate can be calculated as

$$Q_s(\mathbf{r}, E) = \int_E^\infty \eta v_p N_p(\mathbf{r}, E') \delta(z) \frac{d}{dE'} \sigma_{\text{ps}}(E, E') dE', \quad (10)$$

where the suffix “s” indicates secondary species, N_p is the primary CR number density, and $d\sigma_{\text{ps}}(E, E')/dE' = \sigma_{\text{ps}}\delta(E' - E)$ denotes the differential production cross section of a secondary nucleus with energy per nucleon E from a primary nucleus of energy per nucleon E' , where σ_{ps} is the total production cross section of the secondary. Equation (10) then becomes

$$Q_s(\mathbf{r}, E) = \eta v_p \sigma_{\text{ps}} N_p(\mathbf{r}, E) \delta(z). \quad (11)$$

The density of the secondary CRs can be obtained using a similar transport equation as describes the primary CRs (Equation (8)), but with the source term replaced by Equation (11). Their density at $\mathbf{r} = 0$ is given by (S. Thoudam & J. R. Hörandel 2013)

$$N_s(0, 0, E) = \eta v_p \sigma_{\text{ps}} N_p(0, 0, E) \frac{R}{2D_s} \times \int_0^\infty \frac{J_1(KR) dK}{K \coth(KH) + \frac{\eta v_s \sigma_s}{2D_s}}, \quad (12)$$

where $N_s(0, 0, E)$ is given by Equation (9). For the calculation of the secondary particles, it should be mentioned that we only consider primaries from the CR background, but not the primaries originating from the nearby SNRs as they do not have enough time to interact with the ISM before reaching the Earth, as discussed in Section 2.1.

Our study focuses only on boron nuclei as the secondary CR species. They are known to be produced mainly from the spallation of ^{12}C and ^{16}O primaries in the Galaxy. Upon interaction, these primaries generate (^{11}B , ^{10}B) and (^{11}C , ^{10}C) isotopes. The latter subsequently decays into (^{11}B , ^{10}B). For our calculations, we take the secondary production cross sections from U. Heinbach & M. Simon (1995).

2.3. Secondary-to-primary Ratio from Background Cosmic Rays

The secondary-to-primary ratio for background CRs can be calculated from Equation (12). The ratio, $N_s/N_p \propto 1/D_s$, is used to determine the diffusion coefficient in the Galaxy. For

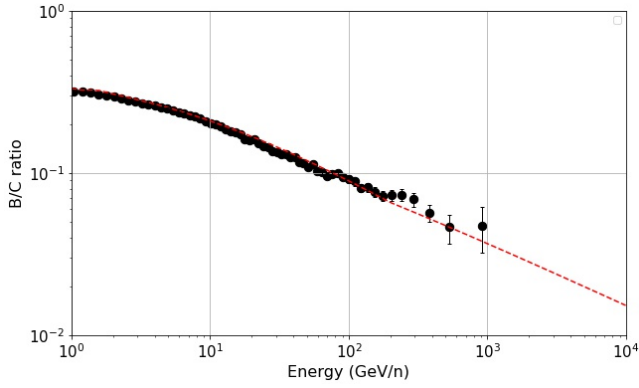


Figure 2. Boron-to-carbon (B/C) ratio for the background CRs (dashed line). Data points are from the AMS-02 experiment (M. Aguilar et al. 2016).

the present study, we model $D(E)$ in the form of

$$D(E) = D_0 \left(\frac{v}{c} \right) \left(\frac{E}{E_0} \right)^\delta, \quad E \leq E_1$$

$$= D_0 \left(\frac{v}{c} \right) \left(\frac{E}{E_1} \right)^{\delta_1} \left(\frac{E_1}{E_0} \right)^\delta, \quad E > E_1, \quad (13)$$

where, again, E is the kinetic energy per nucleon, v is the particle velocity, c is the velocity of light, D_0 is the diffusion constant, and δ (δ_1) are the diffusion indices below (above) the break energy E_1 . Optimizing Equation (13) to boron-to-carbon ratio (B/C) data from the AMS-02 experiment (M. Aguilar et al. 2016), we obtain $D_0 = 1.55 \times 10^{28} \text{ cm}^2 \text{ s}^{-1}$, $\delta = 0.54$, $\delta_1 = 0.40$, and $E_1 = 200 \text{ GeV n}^{-1}$. E_0 is fixed at 3 GeV n^{-1} in the procedure. The result is shown in Figure 2 (dashed line). In a pure diffusion model of CR propagation in the Galaxy such as the one considered in this work, the slight hardening observed in the B/C data above $\sim 100 \text{ GeV n}^{-1}$ requires a change in the diffusion index toward smaller values at high energies. For simplicity, this is often incorporated as a break in $D(E)$ around $100\text{--}300 \text{ GeV n}^{-1}$ (Y. Génolini et al. 2017). A similar behavior of $D(E)$ has also been introduced to explain the hardening in the CR primary spectra above $\sim 200 \text{ GeV n}^{-1}$ on the assumption that there exists a respective break in the turbulence spectrum in the Galaxy (P. Blasi et al. 2012). However, it has been recently argued that a break in the turbulence spectrum is unlikely to introduce a corresponding significant break in the particle spectrum because the “exact” cyclotron wave–particle resonance condition, $p = eB/c k \cos \theta$, also involves the particle’s pitch angle θ , in addition to the wavenumber k and the particle momentum p (M. Malkov et al. 2024). Here, B is the ISM magnetic field, e the charge of an electron, and c the velocity of light. The exact resonance condition allows particles with the same momentum but with different pitch angles to interact with waves of different wavenumbers. This will eventually smear out the effect of the break in the turbulence spectrum on the particle spectrum. Moreover, even if a spectral break in the particle spectrum is formed, the break feature can be smoothened by the diffusion in momentum space which particles experience during their propagation through the Galaxy, unless the break is formed not so far away from Earth (M. Malkov et al. 2024). For the work

presented here, which focuses on explaining the spectral bump (along with the spectral hardening above $\sim 200 \text{ GeV n}^{-1}$) based on local sources, the break in $D(E)$ introduced in Equation (13) will not have a significant effect on the main results. It is also worth mentioning that models involving CR reacceleration in the Galaxy do not require such a break in $D(E)$ in order to explain the B/C data (see, e.g., E. S. Seo & V. S. Ptuskin 1994; S. Thoudam & J. R. Hörandel 2014).

It may be noted that recent measurements of B/C by the CALET (O. Adriani et al. 2022b) and DAMPE (Dampe Collaboration 2022) experiments show an indication of flattening of the ratio above $\sim 1 \text{ TeV}$. Such a flattening may be an effect of the reacceleration of CRs by strong shocks associated with young SNRs during their propagation in the Galaxy (A. Wandel et al. 1987; P. Blasi 2017) or due to the production of secondaries inside the source region from the interaction of primary nuclei with local matter (E. G. Berezhko et al. 2003; R. Cowsik & B. Burch 2010). Neither of these mechanisms will affect the background CR primaries. However, the shape of the background secondaries can be affected, particularly at high energies, due to the generation of an additional component of the secondaries with a source spectrum similar to that of the primaries which is much flatter than that of the secondaries produced in the ISM. In the present study, we neglect the flattening in B/C at TeV energies since it does not affect the major results presented here, which focus on the spectra of the primary CRs and the all-particle spectrum.

2.4. Additional Model Parameters

Considering that the interstellar matter is distributed mostly within the thin Galactic disk, we use the surface matter density instead of the actual number density for our calculations. The average surface density has been taken as $\eta = 5.17 \times 10^{20} \text{ H atoms cm}^{-2}$ (S. Thoudam & J. R. Hörandel 2013), estimated using atomic and molecular hydrogen observations. This value represents an average over a circle of 5 kpc radius from the position of the Sun. We add 10% to this value to take into account the contribution of helium atoms in the ISM. The supernova surface density in Equation (9) is taken as $S = 7.7 \text{ Myr}^{-1} \text{ kpc}^{-2}$, which corresponds to a supernova rate of 0.98 per century in the Galaxy. This value of the supernova rate is consistent with 1.9 ± 1.1 per century as inferred by R. Diehl et al. (2006). Additionally, the effect of solar modulation is included by considering the force-field approximation with a modulation parameter ϕ (L. J. Gleeson & W. I. Axford 1968). We take $\phi = 400 \text{ MV}$, as this value is found to produce an overall good fit to the data below $\sim 10 \text{ GeV n}^{-1}$ for the different CR species considered in this work, as demonstrated in Section 3.1.

3. Cosmic-Ray Spectra Results

In this section, we present the spectra of the individual CR elements obtained with our model, and demonstrate that the presence of nearby SNRs can be responsible for the observed spectral bump between $\sim 1 \text{ TeV}$ and 100 TeV in the proton and the helium spectra. We also obtain the all-particle CR spectrum from our model, and compare it with the observed data up to a few times 10^7 GeV .

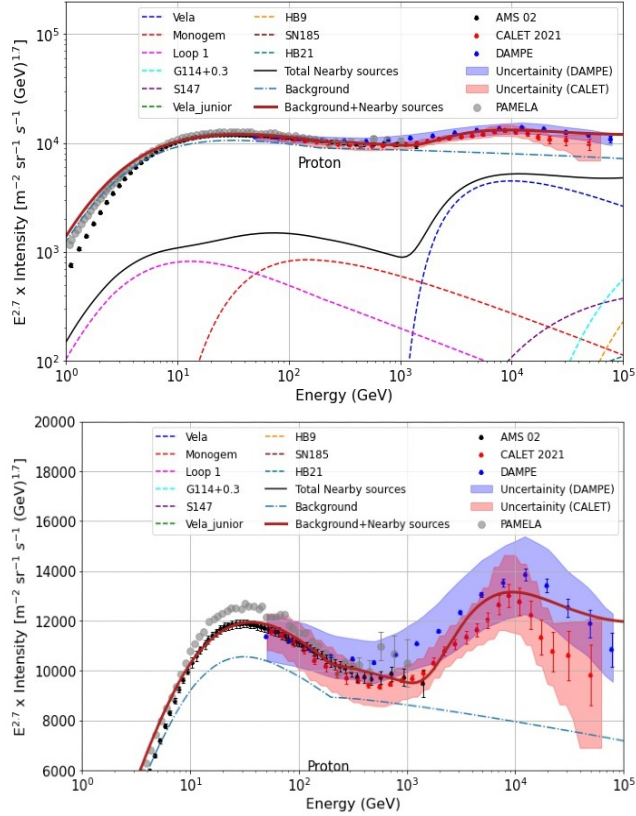


Figure 3. Top panel: proton spectrum in log–log plot. Bottom panel: same spectrum in log–linear plot. The dashed lines show the individual contribution from the nearby SNRs listed in Table 1, the black solid line shows their total contribution, and the dashed–dotted line represents the background component. The red solid line shows the calculated total (nearby+background) proton flux at the Earth. Data points are taken from the AMS-02 (M. Aguilar et al. 2015a), PAMELA (O. Adriani et al. 2011), CALET (O. Adriani et al. 2022a), and DAMPE (Q. An et al. 2019) experiments. The individual contributions of the nearby SNRs are not visible in the bottom panel.

3.1. Individual Element Spectra

Proton and helium spectra. Figures 3 and 4 show the predicted spectra at the Earth for the proton and helium nuclei, respectively. The upper panels of the figures present the spectra in log–log scale, which shows the background contribution (dashed–dotted line) as well as the individual contribution of the nearby SNRs. The black solid line represents the total contribution from the nearby SNRs, and the red solid line represents the total background plus nearby contribution. The lower panels of the figures show the same spectra as in the upper panels, but in log–linear scale. In our calculation, the source index γ and the CR injection efficiency f are kept as model parameters. We allow the individual CR elements to have differing values of (γ, f) , which are optimized based on the observed individual elemental spectra. However, for a given CR species, we constrain the background and the nearby sources to have the same value of γ . In addition, we consider all the nearby sources to have the same values of γ and f for a given CR species. For the protons (Figure 3), we obtain the best-fit values as $\gamma = 2.34$, $f = 16\%$ for the background component, and $f = 25\%$ for the nearby SNRs. For the helium nuclei (Figure 4), we find $\gamma = 2.28$, $f = 1.52\%$ for the background, and $f = 3.1\%$ for the nearby component. We also find that choosing a slightly different value of $D(E)$ for the nearby sources improves the fit quality,

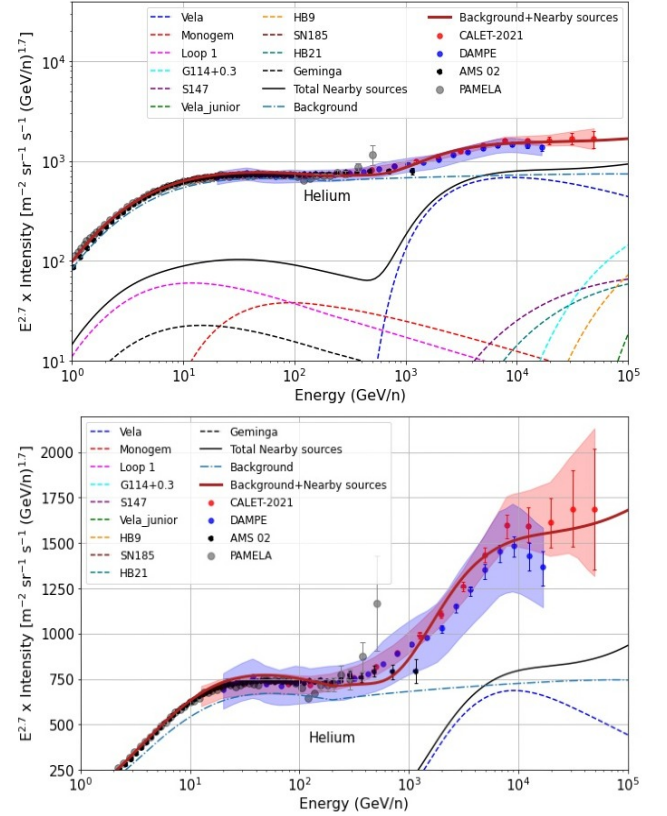


Figure 4. Top panel: helium spectrum in log–log plot. Bottom panel: same spectrum in log–linear plot. The dashed lines show the individual contribution from the nearby SNRs listed in Table 1, the black solid line shows their total contribution, and the dashed–dotted line represents the background component. The red solid line shows the calculated total (nearby+background) helium flux at the Earth. Data points are taken from the AMS-02 (M. Aguilar et al. 2015b), PAMELA (O. Adriani et al. 2011), CALET (O. Adriani et al. 2023), and DAMPE (F. Alemanno et al. 2021) experiments. Among the nearby SNRs, only the contribution of Vela is visible in the bottom panel.

especially in the spectral bump region at $\sim 1\text{--}100\text{ TeV n}^{-1}$ observed by the CALET and the DAMPE experiments. For this reason, we choose $D_0 = 10^{28}\text{ cm}^2\text{ s}^{-1}$, $E_0 = 3\text{ GeV}$, and $\delta = \delta_1 = 0.54$ (i.e., without a break at 200 GeV) for the CR propagation from nearby SNRs. For the background component, we use the value of $D(E)$ as described in Section 2.3. This difference in the diffusion properties is possible if the local region has magnetic turbulence which differs from the Galactic average experienced by the background CRs in the Galaxy.

In our model, the observed spectral bump in the proton and helium spectra at $\sim 1\text{--}100\text{ TeV n}^{-1}$ is explained as a result of the contribution from the nearby SNRs, in particular the Vela SNR. Below $\sim 1\text{ TeV n}^{-1}$, the nearby component contributes significantly less compared to the background flux. The steep rise in the CR flux from Vela at $\sim 1\text{ TeV n}^{-1}$ is mainly due to the energy-dependent CR escape mechanism implemented in our model. CRs below $\sim 1\text{ TeV n}^{-1}$ are mostly still confined with the remnant. There is also an additional effect due to the slow diffusion of CRs at low energies making them unable to reach the Earth within the given time. On the other hand, CRs above $\sim 10\text{ TeV n}^{-1}$, being released at an earlier stage and undergoing faster diffusion, have already passed by the Earth, generating a steep power-law spectrum. It is known that high-energy particles whose diffusion radius, $r_d \sim \sqrt{D(t - T_{\text{esc}})}$, is

much larger than the distance to the observer produce a spectrum that follows $E^{-(\gamma+3\delta_1/2)}$ (S. Thoudam & J. R. Hörandel 2012a). SNRs such as Loop1 and Monogem dominate the nearby contribution below $\sim 1 \text{ TeV n}^{-1}$, while others such as Vela Junior, SN 185, and HB 9 show their contribution only above $\sim 10 \text{ TeV n}^{-1}$, though they remain subdominant with respect to the contribution from Vela.

The contribution from nearby SNRs looks similar between the proton and helium spectra, except that the helium results are slightly shifted toward lower energies. This difference is primarily due to the early escape time of helium nuclei relative to the protons at the same energy per nucleon. In fact, in our model, all the nuclei heavier than protons are released earlier by a factor of $(A/Z)^{-1/\alpha}$ with respect to the protons (see Equation (3)).

During the time CRs are confined inside the remnant, particles can gain energy due to a second-order Fermi acceleration process resulting from their interaction with the magnetic turbulence. The energy gain depends on the level of the magnetic scattering and the confinement time of the particles. Low-energy particles suffer more scattering, and they escape at a later stage of the SNR evolution compared to high-energy particles. Therefore, the energy gain due to the second-order Fermi process is expected to affect mostly particles at low energies. In the following, we present an estimate of the energy gain for protons and its effect on the spectrum at the Earth, considering the Vela SNR as an example.

Cosmic rays remain confined inside the remnant as long as their upstream diffusion length is less than the escape length, as discussed in Section 2.1. Under this condition, the upstream spatial diffusion coefficient at the time particles of energy E escape the remnant is determined as $D_u(E) = \xi R_s(t) v_s(t)$, where $\xi = 0.1$ (L. O. Drury 2011) and $t = t_{\text{esc}}(E) \propto E^{-1/\alpha}$ as given by Equation (3). For the value of $\alpha = 2.4$ adopted in this work, $R_s \propto E^{-0.17}$ and $v_s \propto E^{0.25}$. This gives $D_u(E) \propto E^{0.08}$, which shows a very weak dependence on the escape energy. In other words, the upstream diffusion coefficient at an early time when a high-energy particle escapes is more or less similar to the value when a low-energy particle escapes at a later time. This can be understood from our choice of $\alpha = 2.4$ in the escape time $t_{\text{esc}}(E)$, which incorporates a strong magnetic field amplification where the magnetic field scales with the shock velocity as $B_u \propto v_s^d$, with d as a positive constant (see, e.g., A. R. Bell 2004). At the time when high-energy particles of energy E_1 escape, the shock velocity is large, producing a large B_u and a correspondingly small $D_u(E_1)$. On the other hand, when low-energy particles with energy E_2 start to escape, the shock has already slowed down, lowering the magnetic field amplification and producing a large $D_u(E_2)$ which turns out to be comparable to the value of $D_u(E_1)$. The spatial diffusion coefficient in the downstream is expected to be smaller as the magnetic field downstream is compressed. We take it as $D_d = D_u/4$, where for simplicity we assume a compression factor of 4, which corresponds to strong shocks.⁴ Then, using the relation between the spatial and the momentum diffusion coefficients, $D_d D_p \approx (1/9) p^2 V_A^2$ (where $p = E/c$ is the particle momentum and V_A is the velocity associated with the motion of the magnetic turbulence; A. Thornbury &

L. O. Drury 2014), the momentum diffusion coefficient D_p for the CRs in the downstream can be calculated. The corresponding gain in momentum during the time CRs are confined downstream is determined from $\Delta p \sim \sqrt{D_p t_{\text{esc}}}$, where we assume D_p is constant over time.⁵ This gives an energy gain that decreases with energy as $\Delta E/E \propto E^{-0.25}$, where we have used $\Delta E = \Delta p c$. For $V_A = 100 \text{ km s}^{-1}$, we get $\Delta E/E \sim 8.5\%$ at 1 TeV, which comes down to $\sim 5.0\%$ at 10 TeV. When applied to the nearby SNRs, the energy gain will allow particles to escape at slightly earlier times than they would in the absence of the energy gain, according to Equation (3). This, together with the effect of the energy-dependent diffusion in the ISM, will shift the CR spectrum at the Earth from a nearby SNR toward lower energies. When applied to the Vela SNR, we have found an increase in its proton flux at the Earth by a factor of ~ 1.9 at 1 TeV and ~ 1.1 at 10 TeV with respect to the flux in the absence of the second-order Fermi acceleration process shown in Figure 3. Although this increase at $\lesssim 1 \text{ TeV}$ looks significant for Vela, the effect on the total proton flux (background plus nearby components) will not be significant as the nearby SNRs contribute less than $\sim 10\%$ of the total flux below 1 TeV.

Heavier-element spectra. The spectra for the heavier elements are shown in Figure 5 for carbon, oxygen, and iron nuclei, and in Figure 6 for neon, magnesium, and silicon nuclei. For these elements, the spectra are shown only in log-log scale. The effect of the nearby SNRs looks similar to those found in the proton and helium spectra, showing a bump-like feature at $\sim (1-100) \text{ TeV n}^{-1}$. Except for the source index γ and the CR injection fraction f , all other model parameters remain the same as in the calculation for the proton and helium spectra. Table 2 gives the values of γ and f (for the background and the nearby SNRs) for the different elements used in our calculation.

Similar to the proton and helium results, Vela gives the most significant contribution above $\sim 1 \text{ TeV n}^{-1}$ also in the case of heavier nuclei, producing a signature of spectral hardening at TeV energies. This is in agreement with the observations from the AMS-02 and the CALET experiments. CREAM measurements show large uncertainties at these energies, although a similar trend of spectral hardening seems to be present. Future sensitive measurements at higher energies can provide a crucial check of our prediction for the heavier elements.

3.2. All-particle Spectrum

We calculate the all-particle CR spectrum by combining the spectra of the different elements shown in Figures 3–6. The result is shown in Figure 7 (black solid line) and compared with the available measurements from the IceTop (M. G. Aartsen et al. 2013) and Tibet III (M. Amenomori et al. 2008) experiments. The dashed lines represent the spectra of the individual elements, which are sums of the contribution from the background and the nearby sources. In order to reproduce the knee feature in the observed all-particle spectrum, we consider an exponential cutoff in the source spectrum at $E_c = 4 \times 10^6 Z \text{ GeV}$ in our calculation, where Z is the charge number of the element. The deficit in our model prediction above $\sim 10^7 \text{ GeV}$ possibly indicates the presence of

⁴ The actual compression factor that is required for our calculation will be slightly less than 4 as particle escape happens when the shock starts to slow down.

⁵ In our estimate, we neglect the variation of the spatial diffusion coefficient D_d (and hence of D_p) over time. In reality, the value of D_d (or D_p) is expected to increase (or decrease) with time as the level of the magnetic field amplification goes down with the SNR age.

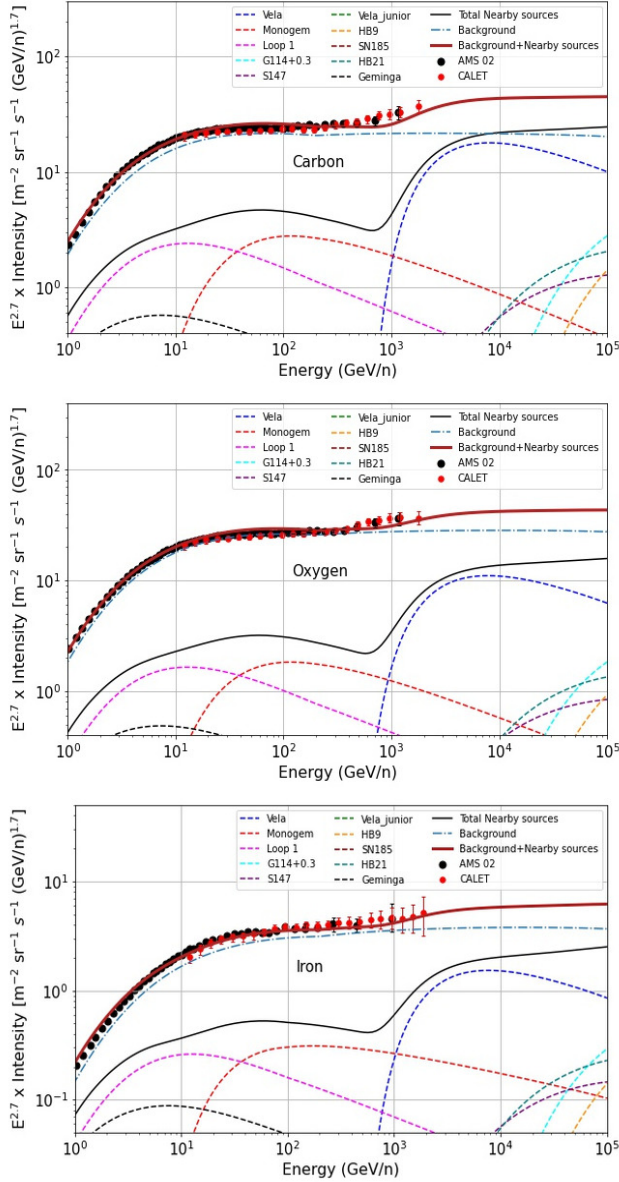


Figure 5. Cosmic-ray energy spectra of the carbon (top), oxygen (middle), and iron (bottom) nuclei. The dashed-dotted line shows the background spectrum, the black solid line shows the total component, the dashed lines show the individual nearby SNRs, and the thick solid maroon line shows the total nearby plus background. The CALET (O. Adriani et al. 2020, 2021) data points have been shifted in energy by +8% for carbon and oxygen, and +6% for iron to minimize the systematic offset with respect to the AMS-02 data (M. Aguilar et al. 2017, 2021).

a second or additional Galactic component (S. Thoudam et al. 2016; S. Bhadra et al. 2024) over the regular sources considered in this work.

4. Discussion

Explanation of the spectral bump. In this study, we have shown that the spectral bump of CR protons and helium nuclei in the TeV region, as recently observed by the CALET and the DAMPE experiments, can be explained as an effect of the contribution from nearby SNRs, especially the Vela SNR. In our model, the spectral bump is explained mainly as a result of the low-energy cutoff due to the energy-dependent escape of CRs from the SNRs and a high-energy falloff of the spectrum

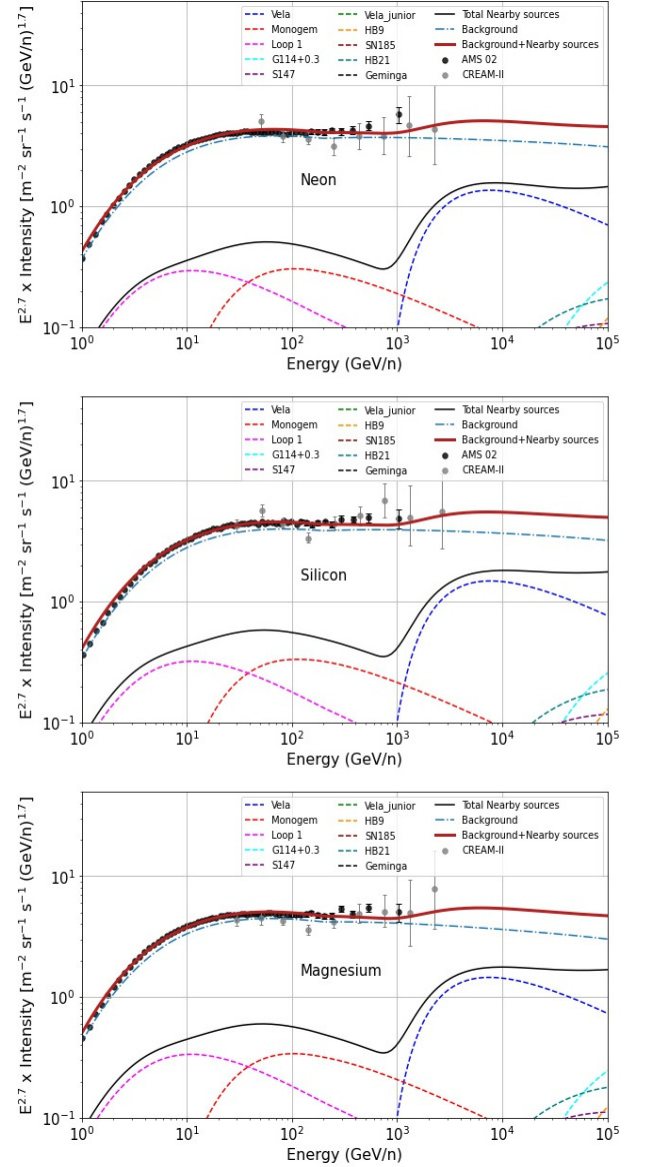


Figure 6. Cosmic-ray energy spectra of the neon (top), silicon (middle), and magnesium (bottom) nuclei. The dashed-dotted line shows the background spectrum, the black solid line shows the total nearby component, the dashed lines show the individual nearby SNRs, and the thick solid maroon line shows the total nearby plus background. The CREAM (H. S. Ahn et al. 2009) data points have been shifted in energy by +11% for neon, silicon, and magnesium to minimize the systematic offset with respect to the AMS-02 data (M. Aguilar et al. 2020).

Table 2

Values of the Source Spectral Index γ and the CR Injection Efficiency f for the Different CR Elements for the Background and the Nearby SNRs

| Elements | Spectral Index (γ) | Injection Fraction ($f \times 10^{49}$ erg) | |
|-----------|-----------------------------|----------------------------------------------|-------------|
| | | Background Sources | Nearby SNRs |
| Proton | 2.34 | 16.0 | 25.0 |
| Helium | 2.28 | 1.52 | 3.10 |
| Carbon | 2.32 | 0.056 | 0.082 |
| Oxygen | 2.31 | 0.062 | 0.070 |
| Iron | 2.32 | 0.010 | 0.010 |
| Silicon | 2.35 | 0.014 | 0.014 |
| Neon | 2.35 | 0.012 | 0.012 |
| Magnesium | 2.38 | 0.014 | 0.016 |

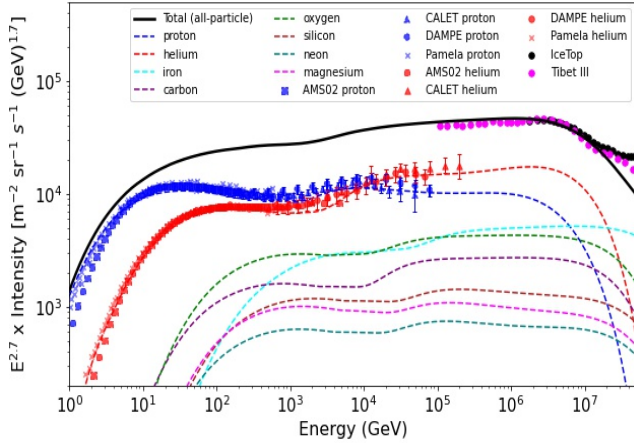


Figure 7. All-particle CR spectrum predicted by our model (black solid line). Each dashed line represents a spectrum of an individual element, which is the sum of the background and the contribution from the nearby SNRs. Individual elemental data are shown only for protons and helium nuclei (same as in Figures 3 and 4). The all-particle data are from the IceTop (M. G. Aartsen et al. 2013) and Tibet III (M. Amenomori et al. 2008) experiments.

due to the energy-dependent propagation of CRs in the Galaxy. These results are in agreement with the earlier findings presented in S. Thoudam & J. R. Hörandel (2012a, 2013) in the context of the observed spectral hardening at $\sim(200\text{--}300)\text{ GeV n}^{-1}$. In contrast, in a recent analysis, A. Li et al. (2024) identified other nearby sources such as Geminga, Monogem, and Loop I as the main contributors to the observed spectral bump. Their calculation differs from our approach in that we consider a more realistic energy-dependent escape of particles from the sources while they assume an energy-independent burst-like injection. Moreover, we consider a more consistent approach by fixing the same source spectral index between the nearby SNRs and the background sources, while A. Li et al. (2024) allows the source index to vary between the nearby SNRs and also with respect to the background component. Our model also reproduces quite well the observed spectra of the heavier elements up to iron, and at the same time predicts a spectral bump for the heavier elements similar to that of the protons and helium nuclei, which can be tested with future observations.

Comparison with other existing models for spectral hardening. The origin of the spectral bump is most likely connected with the spectral hardening observed at $\sim(200\text{--}300)\text{ GeV n}^{-1}$. Several models have tried to explain this spectral hardening, but not all of the models can easily explain the bump. For instance, explanations based on a break in the diffusion coefficient (P. Blasi et al. 2012; N. Tomassetti 2012) or on a hardened source spectrum (Q. Yuan et al. 2011; V. Ptuskin et al. 2013) as well as models based on global reacceleration of CRs by weak shocks in the Galaxy (S. Thoudam & J. R. Hörandel 2014) successfully reproduce the spectral hardening, but they cannot explain the observed bump unless multiple populations of CR sources are invoked (e.g., V. I. Zatsepin & N. V. Sokolskaya 2006; C. Yue et al. 2019). On the other hand, models based on the presence of nearby sources such as the one presented in this work (see also S. Thoudam & J. R. Hörandel 2012a, 2013) or potential nearby CR reacceleration sites as proposed in M. A. Malkov & I. V. Moskalenko (2021) can explain the spectral hardening

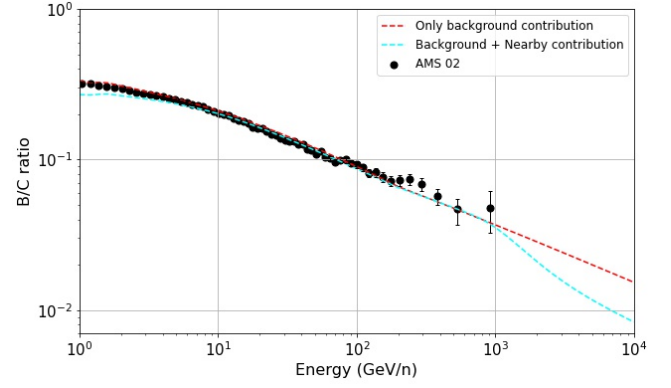


Figure 8. Boron-to-carbon (B/C) ratio in the presence of nearby SNRs (cyan dashed line). The red dashed line shows our model prediction considering only the background sources (same as shown in Figure 2). Data are from the AMS-02 experiment (M. Aguilar et al. 2016).

and the bump at the same time. In our model, these features are generated by CRs from the Vela SNR.

Effect of nearby sources on the B/C ratio. The presence of nearby sources directly affects the secondary-to-primary ratios at the energies where their contribution to the primary CR spectra is significant. Secondary spectra remain unaffected as CR primaries from the nearby sources have to travel far distances in the Galaxy by the time they interact with the ISM and produce secondaries. This leads to a negligible contribution of the secondaries produced by CR primaries from the nearby sources with respect to that produced by the background primaries. The effect will be a suppression in the secondary-to-primary ratios at the energy range where the nearby sources show significant contributions in the primary spectra. This is visible in Figure 8 (cyan line) at energies above $\sim 1\text{ TeV n}^{-1}$. However, at these energies the ratio can also be strongly affected by the reacceleration of secondary CRs by strong shocks in the Galaxy or by the contribution of additional CR secondaries from the interaction of CR primaries inside the sources, neither of which are included in the present study, as discussed in Section 2.3. Therefore, in reality the steepening in the ratio at high energies caused by the presence of nearby sources is expected to remain buried under other dominant effects mentioned above, making it hard to observe.

Effect of nearby sources on cosmic-ray anisotropy. The contribution of the nearby sources is also expected to produce some level of CR anisotropy at the Earth. For a single source dominating the CR flux at a given energy, the total anisotropy δ can be calculated as (e.g., S. Thoudam 2007)

$$\delta(E) = \frac{I_m}{I_T} \delta_m, \quad (14)$$

where I_m denotes the CR intensity from the dominant source at energy E and I_T is the total CR intensity (background plus nearby contribution) at that energy. The anisotropy δ_m from a dominant single source under the diffusion approximation is given by (C. Y. Mao & C. S. Shen 1972)

$$\delta_m = \frac{3D_L}{c} \frac{|\nabla N_m|}{N_m}, \quad (15)$$

where N_m is given by Equation (7) for the dominant source with distance r_m and age t_m , and D_L is the diffusion coefficient

in the local region. For the proton spectrum shown in Figure 3, we get $\delta \sim (1.1\text{--}6) \times 10^{-3}$ over an energy range of (1–100) TeV. These values are approximately a factor of (2–6) higher than the measured dipole anisotropy, which is $\sim(0.5\text{--}1) \times 10^{-3}$ in the same energy range (see A. U. Abeysekara et al. 2019 and references therein). Similar discrepancies were also found in earlier studies (e.g., A. D. Erlykin & A. W. Wolfendale 2006; P. Blasi & E. Amato 2012; S. Thoudam & J. R. Hörandel 2012a). In our model, this discrepancy can be related to the poorly known diffusion coefficient in the local region and uncertainties in the age and distance parameters of the nearby SNRs. Cosmic rays probe large distances in the Galaxy, and therefore the diffusion coefficient determined from the boron-to-carbon data (available only up to a few TeVs n^{-1}) mainly represents the average value in the Galaxy (R. Taillet & D. Maurin 2003; S. Thoudam 2008). This value may differ from that in the local region given that our Sun is located inside the Local Bubble, a hot cavity with an estimated size of ~ 0.5 kpc (P. C. Frisch 2006). Therefore, understanding the local magnetic field structure and its effects on the propagation of CRs can be crucial for the study of anisotropy. Indeed, the small-scale structures observed in anisotropy data at few TeVs are often attributed to the local magnetic field configuration (which is not so well understood) and to the nature of particle scattering in the field, as discussed in L. O. C. Drury & F. A. Aharonian (2008), G. Giacinti & G. Sigl (2012), and M. Ahlers (2014). Moreover, the effect of the heliosphere may be important. At energies below ~ 10 TeV, CRs have a maximum gyroradius of approximately 800 au^6 in a $3 \mu\text{G}$ magnetic field, and therefore their propagation en route to the Earth can be further affected by the heliosphere, which extends up to about a few thousands au (P. Desiati & A. Lazarian 2013; N. V. Pogorelov 2016).




5. Conclusion

We have explored in detail the contribution of nearby SNRs to the observed flux of CRs at the Earth. Based on the results obtained in this work, we conclude that the spectral bump at TeV energies in the proton and helium spectra, as recently observed by the CALET and the DAMPE experiments, is most likely an effect of the contribution of nearby SNRs, in particular the Vela SNR. The contribution of the nearby SNRs is also found to be consistent with the observed spectra of heavier elements from carbon to iron, and also with the all-particle spectrum up to energies beyond the knee when combined with a background CR component originating from the distant sources.

Acknowledgments

S.B. acknowledges the Prime Minister’s Research Fellowship (PMRF) and Govt. of India for financial support. S.T. acknowledges funding from the ADEK grant (grant No. AARE19-224), and Khalifa University grant Nos. ESIG-2023-008 and RIG-S-2023-070.

ORCID iDs

Sourav Bhadra  <https://orcid.org/0000-0002-0044-9751>
 Satyendra Thoudam  <https://orcid.org/0000-0002-7066-3614>
 Prateek Sharma  <https://orcid.org/0000-0003-2635-4643>

References

- Aartsen, M. G., Abbasi, R., Abdou, Y., et al. 2013, *PhRvD*, **88**, 042004
 Abeysekara, A. U., Alfaro, R., Alvarez, C., et al. 2019, *ApJ*, **871**, 96
 Ackermann, M., Ajello, M., Allafort, A., et al. 2013, *Sci*, **339**, 807
 Adriani, O., Akaike, Y., Asano, K., et al. 2020, *PhRvL*, **125**, 251102
 Adriani, O., Akaike, Y., Asano, K., et al. 2021, *PhRvL*, **126**, 241101
 Adriani, O., Akaike, Y., Asano, K., et al. 2022a, *PhRvL*, **129**, 101102
 Adriani, O., Akaike, Y., Asano, K., et al. 2022b, *PhRvL*, **129**, 251103
 Adriani, O., Akaike, Y., Asano, K., et al. 2023, *PhRvL*, **130**, 171002
 Adriani, O., Barbarino, G. C., Bazilevskaya, G. A., et al. 2011, *Sci*, **332**, 69
 Aguilar, M., Aisa, D., Alpat, B., et al. 2015a, *PhRvL*, **114**, 171103
 Aguilar, M., Aisa, D., Alpat, B., et al. 2015b, *PhRvL*, **115**, 211101
 Aguilar, M., Ali Cavazonza, L., Alpat, B., et al. 2017, *PhRvL*, **119**, 251101
 Aguilar, M., Ali Cavazonza, L., Ambrosi, G., et al. 2016, *PhRvL*, **117**, 231102
 Aguilar, M., Ali Cavazonza, L., Ambrosi, G., et al. 2020, *PhRvL*, **124**, 211102
 Aguilar, M., Cavazonza, L. A., Allen, M. S., et al. 2021, *PhRvL*, **126**, 041104
 Ahlers, M. 2014, *PhRvL*, **112**, 021101
 Ahn, H. S., Allison, P., Bagliesi, M. G., et al. 2009, *ApJ*, **707**, 593
 Alemano, F., An, Q., Azzarello, P., et al. 2021, *PhRvL*, **126**, 201102
 Amenomori, M., Bi, X. J., Chen, D., et al. 2008, *ApJ*, **678**, 1165
 An, Q., Asfandiyarov, R., Azzarello, P., et al. 2019, *SciA*, **5**, eaax3793
 Axford, W. I. 1994, *ApJS*, **90**, 937
 Axford, W. I., Leer, E., & Skadron, G. 1977, ICRC (Plovdiv), **11**, 132
 Bell, A. R. 1978, *MNRAS*, **182**, 147
 Bell, A. R. 2004, *MNRAS*, **353**, 550
 Berezhko, E. G. 1996, *Aph*, **5**, 367
 Berezhko, E. G., Ksenofontov, L. T., Ptuskin, V. S., Zirakashvili, V. N., & Völk, H. J. 2003, *A&A*, **410**, 189
 Berezhko, E. G., Pühlhofer, G., & Völk, H. J. 2009, *A&A*, **505**, 641
 Berezhinskii, V. S., & Grigor’eva, S. I. 1988, *A&A*, **199**, 1
 Bernard, G., Delahaye, T., Keum, Y. Y., et al. 2013, *A&A*, **555**, A48
 Bhadra, S., Thoudam, S., Nath, B. B., & Sharma, P. 2024, *ApJ*, **961**, 215
 Biermann, P. L., Becker, J. K., Dreyer, J., et al. 2010, *ApJ*, **725**, 184
 Blandford, R. D., & Ostriker, J. P. 1978, *ApJL*, **221**, L29
 Blasi, P. 2017, *MNRAS*, **471**, 1662
 Blasi, P., & Amato, E. 2012, *JCAP*, **2012**, 011
 Blasi, P., Amato, E., & Serpico, P. D. 2012, *PhRvL*, **109**, 061101
 Büsching, I., Kopp, A., Pohl, M., et al. 2005, *ApJ*, **619**, 314
 Cappiello, C. V., Avis Kozar, N. P., & Vincent, A. C. 2023, *PhRvD*, **107**, 035003
 Caprioli, D., Blasi, P., & Amato, E. 2009, *MNRAS*, **396**, 2065
 Cowsik, R., & Burch, B. 2010, *PhRvD*, **82**, 023009
 Cowsik, R., & Lee, M. A. 1979, *ApJ*, **228**, 297
 DAmpe Collaboration 2022, *SciBu*, **67**, 2162
 Desiati, P., & Lazarian, A. 2013, *ApJ*, **762**, 44
 Dickinson, C. 2018, *Galax*, **6**, 56
 Diehl, R., Halloin, H., Kretschmer, K., et al. 2006, *Natur*, **439**, 45
 Drury, L. O. 2011, *MNRAS*, **415**, 1807
 Drury, L. O. C. 2012, *Aph*, **39**, 52
 Drury, L. O. C., & Aharonian, F. A. 2008, *Aph*, **29**, 420
 Erlykin, A. D., & Wolfendale, A. W. 2006, *Aph*, **25**, 183
 Erlykin, A. D., & Wolfendale, A. W. 2012, *Aph*, **35**, 449
 Faherty, J., Walter, F. M., & Anderson, J. 2007, *Ap&SS*, **308**, 225
 Fesen, R. A., Weil, K. E., Cisneros, I. A., Blair, W. P., & Raymond, J. C. 2018, *MNRAS*, **481**, 1786
 Frisch, P. C. 2006, *Solar Journey: The Significance of Our Galactic Environment for the Heliosphere and Earth* (Dordrecht: Springer)
 Gabici, S., Aharonian, F. A., & Casanova, S. 2009, *MNRAS*, **396**, 1629
 Giacinti, G., & Sigl, G. 2012, *PhRvL*, **109**, 071101
 Gleeson, L. J., & Axford, W. I. 1968, *ApJ*, **154**, 1011
 Globus, N., Allard, D., & Parizot, E. 2015, *PhRvD*, **92**, 021302
 Greisen, K. 1966, *PhRvL*, **16**, 748
 Gvaramadze, V. V. 2006, *A&A*, **454**, 239
 Génolini, Y., Serpico, P. D., Boudaud, M., et al. 2017, *PhRvL*, **119**, 241101
 H. E. S. S. Collaboration, Abdalla, H., Abramowski, A., et al. 2018a, *A&A*, **612**, A6
 H. E. S. S. Collaboration, Abramowski, A., Aharonian, F., et al. 2018b, *A&A*, **612**, A4

⁶ $1 \text{ au} \approx 4.85 \times 10^{-9} \text{ kpc}$.

- H. E. S. S. Collaboration, Aharonian, F., Ait Benkhali, F., et al. 2023, *A&A*, **673**, A148
- Heinbach, U., & Simon, M. 1995, *ApJ*, **441**, 209
- Kelner, S. R., Aharonian, F. A., & Bugayov, V. V. 2006, *PhRvD*, **74**, 034018
- Kobayashi, T., Komori, Y., Yoshida, K., & Nishimura, J. 2004, *ApJ*, **601**, 340
- Lagage, P. O., & Cesarsky, C. J. 1983, *A&A*, **125**, 249
- Lazendic, J. S., & Slane, P. O. 2006, *ApJ*, **647**, 350
- Leahy, D. A., & Tian, W. W. 2007, *A&A*, **461**, 1013
- Letaw, J. R., Silberberg, R., & Tsao, C. H. 1983, *ApJS*, **51**, 271
- Li, A., Liu, W., & Guo, Y. 2024, *Symm*, **16**, 236
- Malkov, M., Moskalenko, I., Diamond, P., & Cao, M. 2024, *AdSpR*, **74**, 4264
- Malkov, M. A., & Drury, L. O. 2001, *RPPh*, **64**, 429
- Malkov, M. A., & Moskalenko, I. V. 2021, *ApJ*, **911**, 151
- Mao, C. Y., & Shen, C. S. 1972, *ChJPh*, **10**, 16
- Maxted, N. I., Filipović, M. D., Sano, H., et al. 2018, *ApJ*, **866**, 76
- Mertsch, P. 2011, *JCAP*, **2011**, 031
- Ohira, Y., Murase, K., & Yamazaki, R. 2011, *MNRAS*, **410**, 1577
- Parizot, E., Marcowith, A., Ballet, J., & Gallant, Y. A. 2006, *A&A*, **453**, 387
- Pogorelov, N. V. 2016, *JPhCS*, **719**, 012013
- Ptuskin, V., Zirakashvili, V., & Seo, E.-S. 2013, *ApJ*, **763**, 47
- Seo, E. S., & Ptuskin, V. S. 1994, *ApJ*, **431**, 705
- Stall, A., Loo, C. K., & Mertsch, P. 2025, *ApJL*, **980**, L21
- Strong, A. W., & Moskalenko, I. V. 1998, *ApJ*, **509**, 212
- Strong, A. W., Moskalenko, I. V., Porter, T. A., et al. 2009, arXiv:0907.0559
- Sushch, I., Hnatyk, B., & Neronov, A. 2011, *A&A*, **525**, A154
- Taillet, R., & Maurin, D. 2003, *A&A*, **402**, 971
- Thornbury, A., & Drury, L. O. 2014, *MNRAS*, **442**, 3010
- Thoudam, S. 2006, *MNRAS*, **370**, 263
- Thoudam, S. 2007, *MNRAS*, **378**, 48
- Thoudam, S. 2008, *MNRAS*, **388**, 335
- Thoudam, S., & Hörandel, J. R. 2012a, *MNRAS*, **421**, 1209
- Thoudam, S., & Hörandel, J. R. 2012b, *MNRAS*, **419**, 624
- Thoudam, S., & Hörandel, J. R. 2013, *MNRAS*, **435**, 2532
- Thoudam, S., & Hörandel, J. R. 2014, *A&A*, **567**, A33
- Thoudam, S., Rachen, J. P., van Vliet, A., et al. 2016, *A&A*, **595**, A33
- Tomassetti, N. 2012, *ApJL*, **752**, L13
- Unger, M., Farrar, G. R., & Anchordoqui, L. A. 2015, *PhRvD*, **92**, 123001
- Vink, J., & Laming, J. M. 2003, *ApJ*, **584**, 758
- Völk, H. J., Berezhko, E. G., & Ksenofontov, L. T. 2005, *A&A*, **433**, 229
- Wandel, A., Eichler, D., Letaw, J. R., Silberberg, R., & Tsao, C. H. 1987, *ApJ*, **316**, 676
- Webber, W. R., & Soutoul, A. 1998, *ApJ*, **506**, 335
- Yar-Uyaniker, A., Uyaniker, B., & Kothés, R. 2004, *ApJ*, **616**, 247
- Yuan, Q., Zhang, B., & Bi, X.-J. 2011, *PhRvD*, **84**, 043002
- Yue, C., Ma, P.-X., Yuan, Q., et al. 2019, *FrPhy*, **15**, 24601
- Zatsepin, G. T., & Kuz'min, V. A. 1966, *JETPL*, **4**, 78
- Zatsepin, V. I., & Sokolskaya, N. V. 2006, *A&A*, **458**, 1